Topological Quantum Walks in Momentum Space with a Bose-Einstein Condensate

Dizhou Xie,[1,*] Tian-Shu Deng,[2,*] Teng Xiao,[1] Wei Gou,[1] Tao Chen,[1] Wei Yi,[2,3,†] and Bo Yan[1,4,5,‡]
[1]Interdisciplinary Center of Quantum Information, State Key Laboratory of Modern Optical Instrumentation, and Zhejiang Province Key Laboratory of Quantum Technology and Device of Physics Department, Zhejiang University, Hangzhou 310027, China
[2]CAS Key Laboratory of Quantum Information, University of Science and Technology of China, Hefei 230026, China
[3]CAS Center For Excellence in Quantum Information and Quantum Physics, Hefei 230026, China
[4]Collaborative Innovation Centre of Advanced Microstructures, Nanjing University, Nanjing 210093, China
[5]Key Laboratory of Quantum Optics, Chinese Academy of Sciences, Shanghai 200800, China

(Received 7 July 2019; accepted 15 January 2020; published 5 February 2020)

We report the experimental implementation of discrete-time topological quantum walks of a Bose-Einstein condensate in momentum space. Introducing stroboscopic driving sequences to the generation of a momentum lattice, we show that the dynamics of atoms along the lattice is effectively governed by a periodically driven Su-Schrieffer-Heeger model, which is equivalent to a discrete-time topological quantum walk. We directly measure the underlying topological invariants through time-averaged mean chiral displacements, which are consistent with our experimental observation of topological phase transitions. We then observe interaction-induced localization in the quantum-walk dynamics, where atoms tend to populate a single momentum-lattice site under interactions that are nonlocal in momentum space. Our experiment opens up the avenue of investigating discrete-time topological quantum walks using cold atoms, where the many-body environment and tunable interactions offer exciting new possibilities.

DOI: 10.1103/PhysRevLett.124.050502

Exploring topological phases is a main theme in modern physics. Characterized by topological invariants that reflect the global geometric properties of the system wave function, topological phases host a range of fascinating features, which are robust to local perturbations and potentially useful for applications in quantum information [1,2]. In addition to conventional topological materials in solid-state systems, topological phenomena also emerge away from equilibrium. For example, topological phenomena exist in non-Hermitian open systems [3–14], quench processes, and periodically driven Floquet systems [15–33], which have stimulated intense interest recently due to the rapid progress in synthetic quantum-simulation platforms such as cold atoms [34–37], photonics [38–51], phononics [52], and superconducting qubits [53].

In particular, photonic topological quantum walks have proved to be a versatile platform for investigating topological phenomena in both unitary [38–45] and nonunitary [47–51] Floquet dynamics. In cold atoms, whereas Floquet topological phases [34] and quantum walks [54] have been respectively implemented, quantum walks with topological properties are yet to be realized. In contrast to photonic quantum walks, where only dynamics of up to two strongly correlated photons have been reported [55,56], the quantum-many-body nature and tunable interactions [57] of cold atoms offer the exciting possibility of exploring topological quantum walks in the presence of many-body entanglement [58] or strong interactions.

Here we report the experimental implementation of discrete-time topological quantum walks in momentum space for a Bose-Einstein condensate (BEC). Building upon the technique of momentum-lattice generation [59–63], we introduce a staggered, time-periodic driving sequence to the Raman-induced tunneling along the lattice, such that dynamics of the condensate atoms is well described by a discrete-time quantum walk that supports Floquet topological phases. Our scheme is in contrast to previous implementations of photonic quantum walks, where the dynamics is driven by the propagation of classical light or photons rather than by Hamiltonians.

We confirm topological properties of the atomic quantum walk by measuring dynamic signatures such as time-averaged mean chiral displacement (A-MCD) [40] and the second-statistical moment [39]. As an illustrative example of the tunability of cold atoms, we experimentally demonstrate the interaction-induced localization in the quantum-walk dynamics, where the degree of localization sensitively depends on the BEC density.

Discrete-time quantum walks in momentum space.—We implement discrete-time quantum walks in momentum space using Raman-induced momentum lattice with periodic driving (see Fig. 1). In previous experiments, momentum lattices have been realized for cold atoms, thanks to the precise control of momentum states with multifrequency Raman beams [59–63]. Here we further introduce periodic switching of the odd- and even-frequency components of

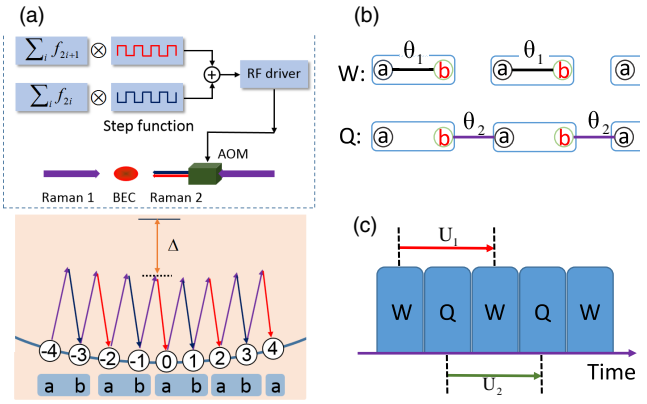

FIG. 1. Experimental implementation of momentum-space discrete-time quantum walks with cold atoms. (a) Atoms in the BEC are coupled by counterpropagating Raman beams. One of the Raman beams (Raman 2) is imprinted with multiple-frequency components via an acoustic-optical modulator (AOM). The odd- and even-frequency components, marked by red and blue arrows, alternate in time, which are controlled by the radio-frequency (rf) driver. The periodically modulated Raman processes couple discretized momentum states, leading to a momentum lattice labeled by $n \in \mathbb{Z}$ with nearest-neighbor Raman-assisted hopping. The staggered Raman couplings enable us to define sublattice sites a and b along the lattice. (b) Illustration of the effective time-evolution operators W and Q. Under W (Q), the intracell (intercell) couplings are turned on along the momentum lattice. (c) Illustration of the two time frames, dictated by Floquet operators U_1 and U_2 (see main text), respectively.

the multifrequency Raman lasers [see Fig. 1(a)]. This gives rise to a stroboscopic switching of the hopping terms between adjacent sites along the momentum lattice. Here the nth site ($n \in \mathbb{Z}$) along the lattice corresponds to the momentum $p_n = n \times 2\hbar k$, where k is the wave vector of the Raman lasers. As illustrated in Fig. 1(a), atoms on site n and $n+1$ are coupled by a pair of Raman beams with an offset frequency $f_n = (2n+1) \times 4E_r/h$, where E_r is the recoil energy. In order to realize the switching of Raman couplings, the offset frequencies are divided into odd and even components depending on the parity of n. While these odd- and even-frequency components are switched on and off by step functions through the rf driver, the effective Hamiltonian for the BEC is given by a periodically driven Su-Schrieffer-Heeger model

$$\hat{H} = \sum_m [w(t)|m,b\rangle\langle m,a| + q(t)|m+1,a\rangle\langle m,b| + \text{H.c.}], \tag{1}$$

where nonresonant Raman couplings are neglected. This would be a good approximation for $\hbar\Omega \ll 4E_r$, whereas typical experimental parameters feature $\hbar\Omega \sim E_r$. While these nonresonant couplings are a major source of imperfection, they do not qualitatively change our results (see Supplemental Material [64]). Here m labels the unit cell, and a and b are the sublattice sites, with $|m,a\rangle$ ($|m,b\rangle$) corresponding to the momentum-lattice site $n = 2m$ ($n = 2m+1$). Importantly, the stepwise Raman-induced hopping rates $w(t)$ and $q(t)$ satisfy $w(t) + q(t) = -\hbar\Omega/2$, where Ω is the Raman-coupling rate and $w(t)$ is given by

$$w(t) = \begin{cases} -\frac{\hbar\Omega}{2}, & jT < t \le jT + t_w \\ 0, & jT + t_w < t \le (j+1)T \end{cases}. \tag{2}$$

Here $j \in \{0,1,2,\ldots.\}$, $T = t_w + t_q$, and t_w and t_q are pulse durations for Raman processes with even- and odd-frequency components, respectively.

Dynamics under Eq. (1) can be mapped to discrete-time quantum-walk dynamics governed by Floquet operators. As illustrated in Fig. 1(b), when the even-frequency Raman coupling is turned on, intracell hopping $w(t)$ in Eq. (1) is finite, while $q(t) = 0$. It follows that the corresponding time-evolution operator $W(\theta_1)$ is

$$W(\theta_1)|m,a(b)\rangle = \cos\theta_1|m,a(b)\rangle + i\sin\theta_1|m,b(a)\rangle, \tag{3}$$

where $\theta_1 = \Omega t_w/2$. Similarly, when the odd-frequency Raman coupling is turned on, intercell hopping $q(t)$ is finite and $w(t) = 0$. The time-evolution operator $Q(\theta_2)$ is

$$Q(\theta_2)|m,a(b)\rangle = \cos\theta_2|m,a(b)\rangle + i\sin\theta_2|m \mp 1,b(a)\rangle, \tag{4}$$

where $\theta_2 = \Omega t_q/2$. Note that the condition $t_w + t_q = T$ translates to $\theta_1 + \theta_2 = \Omega T/2$. The overall dynamics is thus governed by the Floquet operator $U = Q(\theta_2)W(\theta_1)$, which drives the discrete-time quantum walk. We note that the static effective Hamiltonian H_F associated with the Floquet operator is defined through $U = e^{-iH_F T/\hbar}$, which is different from the Hamiltonian (1).

Experimentally, we prepare a ^{87}Rb BEC with $\sim 1 \times 10^5$ atoms in a crossed dipole trap with trapping frequencies $2\pi \times (115, 40, 100)$ Hz. We generate the momentum lattice with a pair of multifrequency Raman lasers at 1064 nm, following the procedure outlined in Ref. [63]. Quantum walks are introduced by a periodic modulation of the Raman pulses. For detection, we turn off the dipole trap and Raman beams and take an absorption image after 20 ms time of flight, from which atomic populations at different momenta are extracted. For all our experiments, we set $\Omega = 2\pi \times 2.3(1)$ and $E_r/\hbar = 2\pi \times 2.03$ kHz, while θ_1 and θ_2 are tuned by adjusting pulse durations t_w and t_q.

A typical experimental measurement for a homogeneous discrete-time quantum-walk dynamics is shown in Fig. 2, where a ballistic spreading of population, typical for discrete-time quantum walks, is observed. Here we fix $T \approx 0.22$ ms and $\theta_1 = \theta_2 = \pi/4$. The experimental observation agrees well with numerical simulations using either the full Hamiltonian (with nonresonant Raman terms) or the

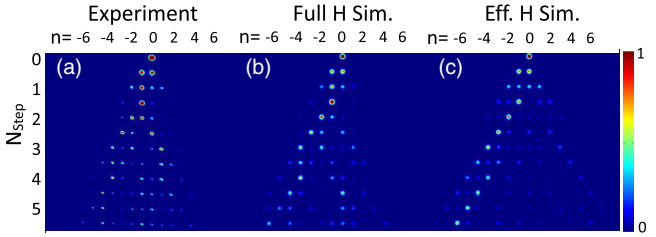

FIG. 2. (a) Experimental demonstration of a typical discrete-time quantum-walk dynamics in momentum space. The color scale indicates atomic population of the corresponding momentum-lattice sites, normalized by the total atomic population detected at each time step. (b),(c) Numerical simulation of the atomic population at each time step driven by (b) the full Hamiltonian [64] and (c) the effective Hamiltonian (1), respectively. For both the experiment and the numerical simulations, the atoms are initialized in the ground state of the BEC with $n = 0$ and are evolved under $(\theta_1, \theta_2) = (\pi/4, \pi/4)$. Deviations of the experimental measurements from numerical simulations are due to experimental decoherence [65].

effective Hamiltonian (1), especially at short times. At long times, deviations become manifest due to decoherence from a range of sources [65].

Detecting topological properties.—Quantum walks governed by $U = Q(\theta_2)W(\theta_1)$ support Floquet topological phases, which are characterized by a pair of winding numbers defined in distinct time frames [66]. As illustrated in Fig. 1(c), these time frames are associated with the Floquet operators

$$U_1 = W\left(\frac{\theta_1}{2}\right)Q(\theta_2)W\left(\frac{\theta_1}{2}\right),$$
$$U_2 = Q\left(\frac{\theta_2}{2}\right)W(\theta_1)Q\left(\frac{\theta_2}{2}\right), \tag{5}$$

which have chiral symmetry $\Gamma U_\alpha \Gamma^{-1} = U_\alpha^{-1}$ $(\alpha = 1, 2)$ with $\Gamma = |a\rangle\langle a| - |b\rangle\langle b|$ and give rise to winding numbers C_1 and C_2, respectively. We note that the nonresonant Raman couplings neglected in (1) can break chiral symmetry and give rise to experimental error (see Supplemental Material [64]). However, these terms are far detuned with two-photon detunings much larger than Ω, such that topological features of the quantum-walk dynamics are still manifest in our experimental data.

Following Ref. [66], we define topological invariants $(C_0, C_\pi) = \{[(C_1 + C_2)/2], [(C_1 - C_2)/2]\}$, which dictate the number of topological edge states with quasienergies $ET/\hbar = 0$ and $ET/\hbar = \pi$, respectively, through the bulk-boundary correspondence. The topological phase diagram of the system is shown in Fig. 3(a), where (C_0, C_π) are plotted as functions of the Raman-coupling parameters (θ_1, θ_2).

To experimentally demonstrate topological features of the momentum-space quantum walk, we experimentally probe (C_0, C_π) and confirm topological phase transitions

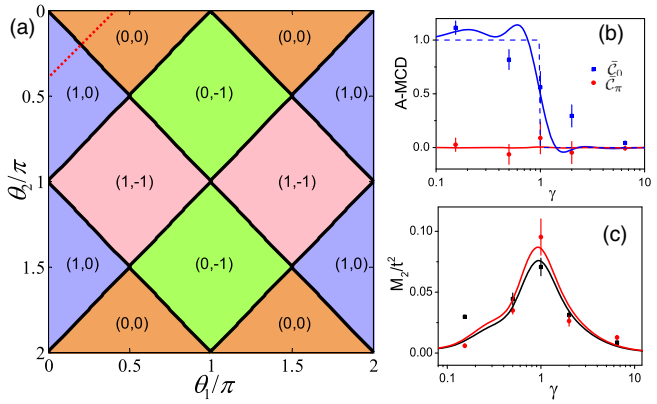

FIG. 3. (a) Topological phase diagram of our discrete-time quantum walk. Topological invariants (C_0, C_π) are shown on the plane of (θ_1, θ_2). The dashed red line indicates the parameters traversed in (b)(c). (b) Experimentally measured A-MCD for a six-step quantum walk, where each data point is averaged over 3 measurements. The dashed blue (red) line shows the variation of C_0 (C_π). (c) Experimentally measured $M_2^{(\alpha)}/N_{\text{step}}^2$ for dynamics governed by U_1 (black) and U_2 (red), respectively. Each data point is averaged over 11 measurements. In (b)(c), the experimental data (dots with error bars) agree well with results from numerical simulations (solid lines) using the effective Hamiltonian (1). Error bars in (b)(c) reflect the standard deviations.

by monitoring dynamics of condensate atoms in momentum space. Quantum walks in different time frames are implemented by applying different sequences of Raman pulses, which correspond to U_1 and U_2, respectively. Here we fix $T \approx 0.16$ ms and adjust t_w and t_q so that $\theta_1 + \theta_2 = 3\pi/8$, as shown by the red dashed line in Fig. 3(a).

First, we directly probe topological invariants (C_0, C_π) by detecting chiral displacements [40]. We initialize atoms in the $n = 0$ state, let them evolve on the lattice, and take time-of-flight images at different time steps. Interestingly, we find that the A-MCD converges much faster to the topological invariant than the commonly used mean chiral displacement (see Supplemental Material [64]). For an N-step quantum walk, the A-MCD is defined as

$$\bar{\mathcal{C}}_\alpha = \frac{2}{N}\sum_{N_{\text{step}}=1}^{N}\sum_{m} m[P_{m,a}^{(\alpha)}(N_{\text{step}}) - P_{m,b}^{(\alpha)}(N_{\text{step}})], \tag{6}$$

where $\alpha \in \{1, 2\}$ indicates the time frame, and $P_{m,a(b)}^{(\alpha)}(N_{\text{step}})$ is the measured atom population in the state $|m, a(b)\rangle$ at the N_{step}th step $(N_{\text{step}} \in \mathbb{N})$ for the dynamics under U_α. Performing the measurements in both time frames, we construct $\bar{\mathcal{C}}_{0,\pi} = \frac{1}{2}(\bar{\mathcal{C}}_1 \pm \bar{\mathcal{C}}_2)$, which should approach $C_{0,\pi}$ in the long-time limit. In our experiment, as shown in Fig. 3(b), the measured A-MCDs agree well with theoretical predictions after a six-step quantum walk.

An important observation of the measured A-MCD is the occurrence of a topological phase transition near $\gamma = 1$

($\gamma = \theta_1/\theta_2$), where the numerically calculated winding numbers C_1 and C_2 undergo abrupt changes. To confirm this, we measure the second-statistical moment $M_2^{(\alpha)}$ characterizing the probability distribution of the walker position, which is defined as

$$M_2^{(\alpha)} = \sum_m m^2 [P_{m,a}^{(\alpha)}(N_{\text{step}}) + P_{m,b}^{(\alpha)}(N_{\text{step}})] \tag{7}$$

for the N_{step}th step. In the long-time limit, $M_2^{(\alpha)}/N_{\text{step}}^2$ should peak at the topological phase boundary under U_α [39], where the corresponding winding number undergoes an abrupt jump. In Fig. 3(c), we show measured $M_2^{(\alpha)}/N_{\text{step}}^2$ after six time steps. The measured peaks in $M_2^{(\alpha)}/N_{\text{step}}^2$ for both time frames are located near $\gamma = 1$, consistent with theoretical predictions. The measured topological invariants and phase transitions are also consistent with edge-state measurement when an open boundary is imposed (see Supplemental Material [64]).

Interaction-induced localization.—A key advantage of an atomic quantum-walk platform is the highly tunable many-body environment and interactions. As an illustrative example, we study the impact of interactions on our quantum-walk dynamics. We consider the short-range, s-wave interactions between ^{87}Rb atoms, which translate to nonlocal interactions on the momentum lattice [60]. Under the Hartree-Fock approximation and taking the mean fields of BEC atoms on each momentum-lattice site, the equations of motion of the system during an interacting quantum-walk dynamics can be written as [64]

$$i\hbar \frac{d}{dt}\Phi = \bar{H}\Phi, \tag{8}$$

where $\Phi = [\phi_{m,a}, \phi_{m,b}]^T$ with $\phi_{m,a}$ ($\phi_{m,b}$) representing the mean-field wave function on the momentum-lattice site $|m, a\rangle$ ($|m, b\rangle$), with the normalization condition $\sum_{m,\sigma} |\phi_{m,\sigma}|^2 = 1$. The matrix elements of $\bar{H}$ are ($\sigma = a, b$)

$$\bar{H}_{m,a;m,b} = \bar{H}_{m,b;m,a} = w(t), \tag{9}$$

$$\bar{H}_{m+1,a;m,b} = \bar{H}_{m,b;m+1,a} = q(t), \tag{10}$$

$$\bar{H}_{m,\sigma;m,\sigma} = U|\phi_{m,\sigma}|^2 + 2U \sum_{m' \neq m,\sigma'} |\phi_{m',\sigma'}|^2. \tag{11}$$

Here the interaction energy $U = g\rho$, where $g = 4\pi\hbar^2 a_s/\mu$, ρ is the BEC density, a_s is the s-wave scattering length, and μ is the atomic mass. In deriving Eq. (8), we use the effective Hamiltonian (1) in addition to the interaction terms (see Supplemental Material [64]).

A direct consequence of interaction, as manifested in Eq. (11), is that the interaction energy between atoms on the same momentum-lattice site is half of that between atoms from different sites. This is due to the presence of an exchange term for two interacting atoms in distinct momentum states [60]. For an interacting BEC, such an effect gives rise to localization of atoms during the quantum-walk dynamics, since the difference in the interaction-energy shift plays the role of an effective detuning that hinders Raman-induced tunnelings. To see the effect, we numerically evolve Eq. (8), assuming a constant U [64], up to the time of an eight-step quantum walk. In Fig. 4(a), we plot the numerically calculated mean distance $\mathcal{D}$, defined through $\mathcal{D} = \sum_m (|2m||\phi_{m,a}|^2 + |2m+1||\phi_{m,b}|^2)$, as a function of $\hbar\Omega/2U$. With decreasing $\hbar\Omega/2U$, interactions dominate the process and $\mathcal{D}$ approaches zero, indicating the localization of atoms in their initial state. In contrast, with increasing $\hbar\Omega/2U$, couplings dominate the process and $\mathcal{D}$ asymptotically approaches $\mathcal{D}_0$, the mean distance for the noninteracting case with $U = 0$. Importantly, a localization-delocalization transition can be roughly identified near $\hbar\Omega/2U \simeq 0.45$, where $\mathcal{D}/\mathcal{D}_0$ takes half the peak value.

To experimentally study the interaction effects, we characterize the interaction energy by $U = g\bar{\rho}$, where $\bar{\rho}$ is the average density of the initial BEC prior to quantum-walk dynamics evaluated with the Thomas-Fermi radius. We first vary $\hbar\Omega$ at a fixed $U/\hbar = 2\pi \times 0.9(1)$ kHz. We evolve the BEC under the Floquet operator U_1 with $\theta_1 = \theta_2 = 3\pi/16$ for two steps, before we take a time-of-flight

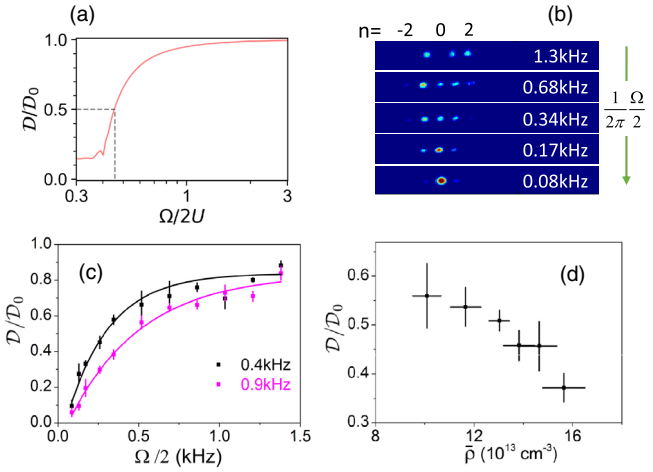

FIG. 4. Interaction-induced localization. (a) Numerically simulated normalized mean distance $\mathcal{D}/\mathcal{D}_0$ as a function of $\hbar\Omega/2U$ after an eight-step quantum walk. (b) Typical time-of-flight images for two-step quantum walks, with $U/\hbar = 2\pi \times 0.9(1)$ kHz. From top to bottom, the Raman-induced tunneling rate $\Omega/2$ varies from $2\pi \times 1.3$ kHz to less than $2\pi \times 100$ Hz. (c) $\mathcal{D}/\mathcal{D}_0$ vs $\Omega/2$ for $U/\hbar = 2\pi \times 0.41(6)$ kHz (black) and $2\pi \times 0.9(1)$ kHz (red). The solid lines are best fits to the experimental results (dots with error bars). (d) Density dependent $\mathcal{D}/\mathcal{D}_0$. The coupling strength is $\Omega/2 = 2\pi \times 0.35$ kHz. The BEC density is decreased by holding BEC in the dipole trap for a long time. The trap frequencies of the dipole trap are $2\pi \times (214, 61, 220)$ Hz.

image of the atoms. Figure 4(b) shows a typical image for various values of $\Omega/2$ ranging from $2\pi \times 1.3$ kHz to less than $2\pi \times 100$ Hz. Apparently, the atoms become more and more localized at their initial lattice site $|0, a\rangle$ as the rate $\hbar\Omega/2U$ decreases. In Fig. 4(c), we show the measured the normalized mean distance $\mathcal{D}/\mathcal{D}_0$ as a function of $\Omega/2$ for different U. Whereas both curves are more smooth compared to the numerically simulated curve in Fig. 4(a), our experimental results are consistent with the numerical prediction that a localization-delocalization transition occurs near $\hbar\Omega/2U \simeq 0.45$. The difference between Figs. 4(a) and 4(c) originates from the finite time of the quantum-walk dynamics, as well as from the spatially nonuniform U in our experiment.

To confirm that the observed localization in the quantum-walk dynamics is unequivocally induced by interactions, we vary $\bar{\rho}$ by only holding the BEC in the dipole trap for different durations, prior to the quantum-walk experiment. This allows us to directly examine the density dependence of the localization with a fixed $\Omega/2 = 2\pi \times 0.35(2)$ kHz. As shown in Fig. 4(d), the normalized mean distance $\mathcal{D}/\mathcal{D}_0$ sensitively depends on the BEC density at the trap center, with increasing localization for larger densities. We therefore conclude that we have indeed observed the interaction-induced localization in quantum-walk dynamics of a BEC in the momentum space. Finally, we note that for our experiments characterizing topological features, $U/\hbar \approx 2\pi \times 0.6(1)$ kHz and $\hbar\Omega/2U \simeq 2$, such that the localization effect due to interactions is negligible. In the future, it would be interesting to explore the interplay of topology and interaction based on our platform.

Discussion.—We experimentally implement a stroboscopic driving of ultracold atoms on a momentum lattice, thus realizing discrete-time quantum-walk dynamics using cold atoms. The accessible number of time steps in our experiment is affected by the finite size and inhomogeneous density distribution of the BEC in the trapping potential. Such inhomogeneity leads to broadening and inhomogeneous interactions in momentum space, which give rise to decoherence in the dynamics. A practical solution is to further weaken the trapping potential by holding the BEC with a gradient magnetic field that compensates the gravity. Our scheme offers exciting possibilities of exploring topological quantum-walk dynamics in the context of strongly correlated many-body systems with tunable interatomic interactions or strong many-body entanglement [58].

We are grateful to Ying Hu for helpful comments. We acknowledge the support from the National Key R&D Program of China under Grant No. 2018YFA0307200, National Natural Science Foundation of China under Grants No. 91636104, No. 11974331, and No. 91736209, Natural Science Foundation of Zhejiang province under Grant No. LZ18A040001, and the Fundamental Research Funds for the Central Universities. W. Y. acknowledges support from the National Key Research and Development Program of China (Grants No. 2016YFA0301700 and No. 2017YFA0304100).

*These authors contributed equally to this work.
†wyiz@ustc.edu.cn
‡yanbohang@zju.edu.cn

[1] M. Z. Hasan and C. L. Kane, Rev. Mod. Phys. **82**, 3045 (2010).
[2] X.-L. Qi and S.-C. Zhang, Rev. Mod. Phys. **83**, 1057 (2011).
[3] M. S. Rudner and L. S. Levitov, Phys. Rev. Lett. **102**, 065703 (2009).
[4] K. Esaki, M. Sato, K. Hasebe, and M. Kohmoto, Phys. Rev. B **84**, 205128 (2011).
[5] S.-D. Liang and G.-Y. Huang, Phys. Rev. A **87**, 012118 (2013).
[6] B. Zhu, R. Lü, and S. Chen, Phys. Rev. A **89**, 062102 (2014).
[7] T. E. Lee, Phys. Rev. Lett. **116**, 133903 (2016).
[8] S. Yao and Z. Wang, Phys. Rev. Lett. **121**, 086803 (2018).
[9] S. Yao, F. Song, and Z. Wang, Phys. Rev. Lett. **121**, 136802 (2018).
[10] F. K. Kunst, E. Edvardsson, J. C. Budich, and E. J. Bergholtz, Phys. Rev. Lett. **121**, 026808 (2018).
[11] Z. Gong, Y. Ashida, K. Kawabata, K. Takasan, S. Higashikawa, and M. Ueda, Phys. Rev. X **8**, 031079 (2018).
[12] K. Kawabata, K. Shiozaki, M. Ueda, and M. Sato, Phys. Rev. X **9**, 041015 (2019).
[13] H. Zhou and J. Y. Lee, Phys. Rev. B **99**, 235112 (2019).
[14] A. Ghatak and T. Das, J. Phys. Condens. Matter **31**, 263001 (2019).
[15] T. Kitagawa, E. Berg, M. Rudner, and E. Demler, Phys. Rev. B **82**, 235114 (2010).
[16] L. Jiang, T. Kitagawa, J. Alicea, A. R. Akhmerov, D. Pekker, G. Refael, J. I. Cirac, E. Demler, M. D. Lukin, and P. Zoller, Phys. Rev. Lett. **106**, 220402 (2011).
[17] J. Eisert, M. Friesdorf, and C. Gogolin, Nat. Phys. **11**, 124 (2015).
[18] M. D. Caio, N. R. Cooper, and M. J. Bhaseen, Phys. Rev. Lett. **115**, 236403 (2015).
[19] L. D'Alessio and M. Rigol, Nat. Commun. **6**, 8336 (2015).
[20] M. S. Rudner, N. H. Lindner, E. Berg, and M. Levin, Phys. Rev. X **3**, 031005 (2013).
[21] N. Goldman and J. Dalibard, Phys. Rev. X **4**, 031027 (2014).
[22] A. C. Potter, T. Morimoto, and A. Vishwanath, Phys. Rev. X **6**, 041001 (2016).
[23] V. Khemani, A. Lazarides, R. Moessner, and S. L. Sondhi, Phys. Rev. Lett. **116**, 250401 (2016).
[24] M. Heyl, A. Polkovnikov, and S. Kehrein, Phys. Rev. Lett. **110**, 135704 (2013).
[25] J. C. Budich and M. Heyl, Phys. Rev. B **93**, 085416 (2016).
[26] Z. Huang and A. V. Balatsky, Phys. Rev. Lett. **117**, 086802 (2016).
[27] Y. Hu, P. Zoller, and J. C. Budich, Phys. Rev. Lett. **117**, 126803 (2016).

[28] J. H. Wilson, J. C. W. Song, and G. Refael, Phys. Rev. Lett. **117**, 235302 (2016).

[29] C. Wang, P. Zhang, X. Chen, J. Yu, and H. Zhai, Phys. Rev. Lett. **118**, 185701 (2017).

[30] C. Yang, L. Li, and S. Chen, Phys. Rev. B **97**, 060304(R) (2018).

[31] Z. Gong and M. Ueda, Phys. Rev. Lett. **121**, 250601 (2018).

[32] L. Zhang, L. Zhang, S. Niu, and X.-J. Liu, Sci. Bull. **63**, 1385 (2018).

[33] X. Qiu, T.-S. Deng, Y. Hu, P. Xue, and W. Yi, iScience **20**, 392 (2019).

[34] G. Jotzu, M. Messer, R. Desbuquois, M. Lebrat, T. Uehlinger, D. Greif, and T. Esslinger, Nature (London) **515**, 237 (2014).

[35] N. Fläschner, B. S. Rem, M. Tarnowski, D. Vogel, D.-S. Lühmann, K. Sengstock, and C. Weitenberg, Science **352**, 1091 (2016).

[36] N. Fläschner, D. Vogel, M. Tarnowski, B. S. Rem, D.-S. Lühmann, M. Heyl, J. C. Budich, L. Mathey, K. Sengstock, and C. Weitenberg, Nat. Phys. **14**, 265 (2018).

[37] W. Sun, C.-R. Yi, B.-Z. Wang, W.-W. Zhang, B. C. Sanders, X.-T. Xu, Z.-Y. Wang, J. Schmiedmayer, Y. Deng, X.-J. Liu, S. Chen, and J.-W. Pan, Phys. Rev. Lett. **121**, 250403 (2018).

[38] T. Kitagawa, M. A. Broome, A. Fedrizzi, M. S. Rudner, E. Berg, I. Kassal, A. Aspuru-Guzik, E. Demler, and A. G. White, Nat. Commun. **3**, 882 (2012).

[39] F. Cardano, M. Maffei, F. Massa, B. Piccirillo, C. de Lisio, G. De Filippis, V. Cataudella, E. Santamato, and L. Marrucci, Nat. Commun. **7**, 11439 (2016).

[40] F. Cardano, A. DErrico, A. Dauphin, M. Maffei, B. Piccirillo, C. de Lisio, G. De Filippis, V. Cataudella, E. Santamato, L. Marrucci, M. Lewenstein, and P. Massignan, Nat. Commun. **8**, 15516 (2017).

[41] S. Barkhofen, T. Nitsche, F. Elster, L. Lorz, A. Gábris, I. Jex, and C. Silberhorn, Phys. Rev. A **96**, 033846 (2017).

[42] X.-Y. Xu, Q.-Q. Wang, W.-W. Pan, K. Sun, J.-S. Xu, G. Chen, J.-S. Tang, M. Gong, Y.-J. Han, C.-F. Li, and G.-C. Guo, Phys. Rev. Lett. **120**, 260501 (2018).

[43] B. Wang, T. Chen, and X. Zhang, Phys. Rev. Lett. **121**, 100501 (2018).

[44] C. Chen, X. Ding, J. Qin, Y. He, Y.-H. Luo, M. C. Chen, C. Liu, X.-L. Wang, W.-J. Zhang, H. Li, L.-X. You, Z. Wang, D.-W. Wang, B. C. Sanders, C.-Y. Lu, and J.-W. Pan, Phys. Rev. Lett. **121**, 100502 (2018).

[45] X.-Y. Xu, Q.-Q. Wang, M. Heyl, J. C. Budich, W.-W. Pan, Z. Chen, M. Jan, K. Sun, J.-S. Xu, Y.-J. Han, C.-F. Li, and G.-C. Guo, Light Sci. Appl. **9**, 7 (2020).

[46] S. Weimann, M. Kremer, Y. Plotnik, Y. Lumer, S. Nolte, K. G. Makris, M. Segev, M. C. Rechtsman, and A. Szameit, Nat. Mater. **16**, 433 (2017).

[47] L. Xiao, X. Zhan, Z. H. Bian, K. K. Wang, X. Zhang, X. P. Wang, J. Li, K. Mochizuki, D. Kim, N. Kawakami, W. Yi, H. Obuse, B. C. Sanders, and P. Xue, Nat. Phys. **13**, 1117 (2017).

[48] X. Zhan, L. Xiao, Z. Bian, K. Wang, X. Qiu, B. C. Sanders, W. Yi, and P. Xue, Phys. Rev. Lett. **119**, 130501 (2017).

[49] J. M. Zeuner, M. C. Rechtsman, Y. Plotnik, Y. Lumer, S. Nolte, M. S. Rudner, M. Segev, and A. Szameit, Phys. Rev. Lett. **115**, 040402 (2015).

[50] K. Wang, X. Qiu, L. Xiao, X. Zhan, Z. Bian, W. Yi, and P. Xue, Phys. Rev. Lett. **122**, 020501 (2019).

[51] K. Wang, X. Qiu, L. Xiao, X. Zhan, Z. Bian, B. C. Sanders, W. Yi, and P. Xue, Nat. Commun. **10**, 2293 (2019).

[52] W. Zhu, X. Fang, D. Li, Y. Sun, Y. Li, Y. Jing, and H. Chen, Phys. Rev. Lett. **121**, 124501 (2018).

[53] X.-Y. Guo, C. Yang, Y. Zeng, Y. Peng, H.-K. Li, H. Deng, Y.-R. Jin, S. Chen, D. Zheng, and H. Fan, Phys. Rev. Applied **11**, 044080 (2019).

[54] S. Dadras, A. Gresch, C. Groiseau, S. Wimberger, and G. S. Summy, Phys. Rev. Lett. **121**, 070402 (2018).

[55] A. Schreiber, A. Gabris, P. P. Rohde, K. Laiho, M. Stefanak, V. Potocek, C. Hamilton, I. Jex, and C. Silberhorn, Science **336**, 55 (2012).

[56] Z. Yan *et al.*, Science **364**, 753 (2019).

[57] C. Chin, R. Grimm, P. Julienne, and E. Tiesinga, Rev. Mod. Phys. **82**, 1225 (2010).

[58] X.-Y. Luo, Y.-Q. Zou, L.-N. Wu, Q. Liu, M.-F. Han, M. K. Tey, and L. You, Science **355**, 620 (2017).

[59] E. J. Meier, F. A. An, and B. Gadway, Phys. Rev. A **93**, 051602(R) (2016).

[60] F. A. An, E. J. Meier, J. Ang'ong'a, and B. Gadway, Phys. Rev. Lett. **120**, 040407 (2018).

[61] E. J. Meier, F. A. An, and B. Gadway, Nat. Commun. **7**, 13986 (2016).

[62] E. J. Meier, F. A. An, A. Dauphin, M. Maffei, P. Massignan, T. L. Hughes, and B. Gadway, Science **362**, 929 (2018).

[63] D. Xie, W. Gou, T. Xiao, B. Gadway, and B. Yan, npj Quantum Inf. **5**, 55 (2019).

[64] See Supplemental Material at http://link.aps.org/supplemental/10.1103/PhysRevLett.124.050502 for the derivation of the effective Hamiltonian and the topological invariants, additional simulation and experimental data demonstrating A-MCDs, the comparison between the full and effective Hamiltonians, the detection of topological edge states, and discussion on the impact of interaction.

[65] Experimental error and decoherence come from a range of sources, including thermal atoms, uneven light distribution, phase fluctuations of the Raman lasers, and population of unwanted momentum states coupled by nonresonant Raman processes or by trapping potentials.

[66] J. K. Asbóth and H. Obuse, Phys. Rev. B **88**, 121406(R) (2013).